THE JOURNAL OF PHYSICAL CHEMISTRY C

pubs.acs.org/JPCC Article

Melting and Structural Dynamics of Indium Nanoparticles Embedded in Aluminum

Yueli Zhang, Hui Xiong, and Hani E. Elsayed-Ali*

Cite This: J. Phys. Chem. C 2020, 124, 19340−19347 Read Online

ACCESS | Metrics & More | Article Recommendations

ABSTRACT: The structural response and melting of indium nanoparticles embedded in the ultrathin aluminum film were studied for slow thermal heating and for ultrafast laser heating using electron diffraction. The nanoparticles were prepared by magnetron sputtering. For slow heating, the indium nanoparticles lost their structural order ∼19 K below the bulk melting point of indium. Significant undercooling was observed when the nanoparticles were cooled. For ultrafast heating using a 110 fs laser pulse, a subset of the nanoparticles was superheated in the range of 1.15−1.40 T_m when heated from 352 K. The temporal response of the indium nanoparticles to ultrafast laser excitation was found to be anisotropic.

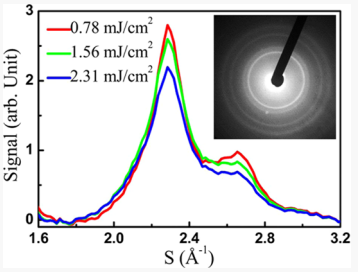

1. INTRODUCTION

Solids with reduced dimensionalities, such as nanoparticles (NPs), have properties that can deviate from their bulk materials. Among the properties that depend on size is the melting point, which is reduced with NP size.[1−5] Understanding the melting of NPs is important for the development of better models of phase transitions at the nanoscale and for the applications of NPs at elevated temperatures. When the size of a solid particle decreases, its surface-to-volume ratio increases. As a result, surface atoms play a major role in the structure of NPs. Buffat and Borel showed that, for gold nanoparticles, the melting point reduction reaches hundreds of degrees below the bulk melting point (T_m) of gold.[6] Since then, a deeper understanding of size-dependent melting has been achieved.[2,3,7−11] The presence of surface melting, in which a surface liquid like layer can coexist with a solid core at a temperature far below T_m, is well demonstrated.[12]

If surface melting is suppressed, then the solid can be superheated up to a temperature that depends on the material properties and on the heating rate.[13] Thin platelets with extensive {0001} surfaces for Bi and {111} for Pb were superheated at slow heating rates up to 7 and 2 K for Bi and Pb, respectively.[14,15] Reflection high-energy electron diffraction (RHEED) study of Pb NPs on graphite revealed that a fraction of the NPs is superheated by (4−12) ± 2 K above T_m.[16] The superheating of {111}-faceted polyhedral Pb crystallites on graphite by 3 K was reported.[17] An ensemble of Bi NPs with size in the range of 20−150 nm, grown on a carbon film, showed superheating by at least 5 K, as detected by the change in the NP shape from platelets to compact polyhedrons.[18] In time-resolved RHEED studies of surfaces heated by ∼120 ps laser pulses (heating rates ∼10^{11} K/s), superheating by ∼120, ∼90, and 73 ± 9 K of the Pb(111), Bi(0001), and In(111) surfaces, respectively, were observed.[13,19,20] NPs embedded in a crystal, or coated with an immiscible low-energy coherent interface, can be superheated above its T_m to a temperature that is dependent on the interface and the heating rate.[21−27]

Indium is one of a few elements with a very low vapor pressure at its T_m (≪10^{-11} Torr)[28] and has a relatively low T_m = 429.75 K. The low vapor pressure at T_m minimizes shape changes due to evaporation as the temperature is raised, resulting in a stable NP shape and size near T_m. Also, the low T_m and the strong absorption of In in the optical and near-IR wavelengths reduce the experimental requirements for continuous heating and pulsed laser heating, respectively. Indium has a tetragonal structure with a = 0.325 nm and c = 0.495 nm.[29] Like most metals, In has a positive Hamaker constant (H), which is a constant that relates the residual interaction between the solid−liquid and liquid−vapor interfaces to the formation of a quasi-liquid surface layer as the temperature is raised to near T_m.[30] A positive H at T_m is normally associated with crystals with surfaces that premelt and undergo positive volume change upon melting, as is the case for most elements.

Previous studies of the melting point of In NPs using scanning calorimetry and scanning tunneling microscopy have shown that NPs melt below T_m and their melting point is inversely proportional to the particle size.[2,31] For In NPs embedded in an Al matrix, the melting point was found higher than T_m of In when the In NPs have an epitaxial orientation

Received: June 1, 2020
Revised: August 3, 2020
Published: August 4, 2020

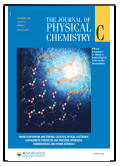

https://dx.doi.org/10.1021/acs.jpcc.0c04950
J. Phys. Chem. C 2020, 124, 19340−19347

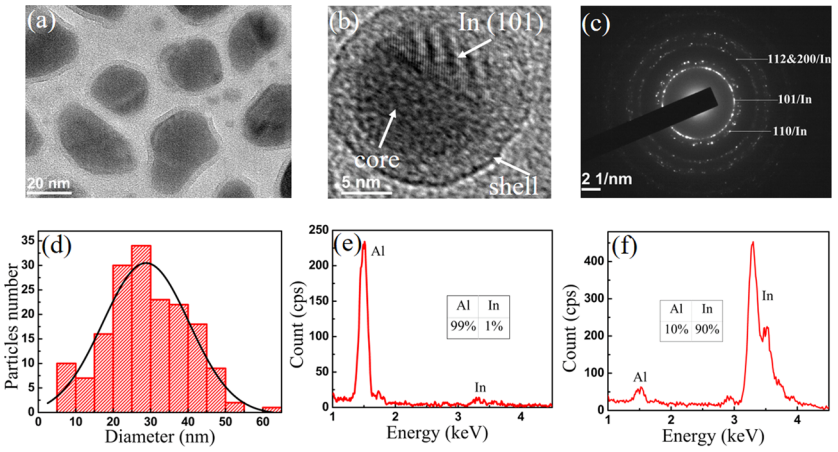

Figure 1. TEM images of In NPs embedded in Al films deposited on carbon-coated TEM grids. (a, b) Core−shell structure of the NPs. (c) Selected area electron diffraction showing only In diffraction orders. The size distribution of the In NPs (d) and EDS in the area without an NP (e) with an NP (f). The measured coverage ratio is ∼56%, and the diameter of the NP is calculated based on area approximation of πr^2. The NPs size is mostly concentrated at a range of 29 ± 14 nm under the Gaussian curve fitting.

with the Al matrix such as $\{111\}_{Al} \parallel \{111\}_{In}$ and $\langle 110\rangle_{Al} \parallel \langle 110\rangle_{In}$. The In NPs were found to have the shape of truncated octahedrals bounded by $\{111\}_{Al}$ and $\{100\}_{Al}$.[21,32] The In NP melting point was lower than T_m when they were situated at the grain boundaries of the Al matrix or were randomly oriented in the surrounding Al.[21,32] These studies of the melting of In NPs embedded in Al were investigated by differential scanning calorimetry for the melting temperature and by transmission electron microscopy (TEM) for morphology and structure, and they were all conducted under slow thermal heating on a hot stage.

It is now well understood that the superheating of the solid phase depends on factors that include the material properties,[30,33] the surface orientation,[34,35] the surface interface,[1,36] and the rate of heating.[26,27,33,37] Higher heating rates can achieve higher superheating of a crystal due to limits on the rate of nucleation and growth of the melt. The maximum superheating temperature is, generally, assumed to be a fundamental limit of material properties, as stated in Born's mechanical instability.[26,33,38] Realization and observation of high degrees of superheated solids are difficult due to the limitations on the heating rate and the difficulty in observing the material structure with high time resolution. Ultrafast lasers have been used to heat materials at heating rates that can be extremely high. However, for subpicosecond laser irradiation, uniform heating is achieved over a depth of about the laser skin depth in the material. Ballistic transport of hot electrons, and for insulators and semiconductors ballistic phonons, can enhance the uniform heating depth. In metals, thermal diffusion can become important only on a time scale in the order of hundreds of ps to ns and longer. Therefore, for materials with strong absorption at the laser wavelength, such as metals, uniform laser heating is not achievable, on the several ps time scale, over a depth much larger than the skin depth of the laser radiation in the material.

Probing the structure of the material with ultrafast time resolution is limited to a few structural probes that are mainly based on diffraction, for example, X-ray and electron diffraction. Time-resolved electron diffraction has been used to investigate surface melting and superheating.[13,19,20,34] Electron diffraction is highly sensitive to the structure of solids in reduced dimensions (e.g., surfaces, NPs, and nanosheets) and provides a direct probe of the structure factor, the lattice spacing, and the mean-square lattice vibrational amplitude.[39,40]

We report on the ultrafast electron diffraction (UED) study of laser-heated 29 ± 14 nm In NPs embedded in ultrathin Al films. The lattice structural evolution is studied by measuring changes in the Bragg diffraction peak intensity and position. For a slow heating rate of ∼1 K/min using a resistively heated stage, the melting point of the embedded In NPs is ∼19 K lower than the T_m of In. For ultrafast laser heating (10^{15} K/s), a subset of the In NPs is superheated in the range of 1.15−1.40 T_m when heated starting from 352 K. The temporal response of the In NPs for the (101) and (110) orders is found to be anisotropic.

2. METHODS

The In NPs embedded in Al were prepared by sputter deposition on a standard copper TEM grids coated with a ∼10 nm carbon film. A multitarget ATC Orion 5 RF/DC sputtering system from AJA International was used to sputter Al and In from 99.999% targets from Kurt J. Lesker. First, an Al thin film was deposited, by DC magnetron sputtering, on the carbon-coated grid with a ∼0.1 Å/s deposition rate at 3.0×10^{-3} Torr argon background pressure. About 8 nm Al was deposited on the carbon. Then, ∼20 nm In was deposited on the Al film with a ∼0.3 Å/s deposition rate at the same argon background pressure, followed by another ∼8 nm layer of Al. The deposition rate was calibrated prior to NP fabrication using a quartz crystal thickness monitor that was positioned at the TEM grid location. After deposition, the samples were placed in the UED chamber, while a sample from the same deposition run was studied by a JEM-2100F (JEOL), 200 kV field emission transmission electron microscope (TEM) equipped with INCAx-sight (Oxford Instruments) energy dispersive spectroscopy (EDS) to investigate the NP shape, size distribution, and chemical composition at different locations in the NP.

In the UED system used in the present study, the electron pulse was generated by photoemission from a ∼30 nm silver photocathode film deposited on a sapphire window. The photocathode was biased at −25 kV and excited by 400 nm laser pulses generated by the frequency doubling of the 800 nm, 110 fs pulse duration Ti:sapphire laser. The laser was

https://dx.doi.org/10.1021/acs.jpcc.0c04950
J. Phys. Chem. C 2020, 124, 19340−19347

operated at a 1 kHz repetition rate. The generated electrons were accelerated toward a grounded anode and then collimated by a set of electromagnet coils located outside the vacuum chamber. The samples were mounted on a resistively heated stage. The sample temperature was measured by a thermocouple placed near the edge of the sample. A temperature controller was used to maintain the sample temperature. The thermocouple was calibrated based on the boiling and freezing points of water. The temperature calibration error was estimated to be ±1 K, which mainly came from the distance of the thermocouple from the probed sample region. The sample was heated by the fundamental 800 nm laser pulse. The fluence of the heating laser pulse was controlled by a combination of a half-waveplate and a thin film polarizer. The pump laser beam was focused on the sample to a spot of ∼2.5 mm full width at half maximum (FWHM), while the electron pulse on the sample had a diameter of a few hundred micrometers. The delay time between the pump laser and probe electrons was controlled by an optical translation stage with submicrometer resolution. The temporal resolution of the UED setup was ∼1.5 ps at the photocathode voltage and the laser excitation used. More details on our UED setup were previously discussed.[41,42]

The diffraction pattern was detected by a pair of microchannel plates that were proximity-coupled to a phosphor screen. The phosphor screen was lens-coupled to a CCD camera with 1024 × 1024 pixels. After acquiring the diffraction pattern by the CCD camera, the image was processed by a MATLAB program that we developed, which allowed for radial averaging and background fitting and subtraction using a wavelet transform.[43] The diffraction peak intensity, peak position, and peak width were also extracted by the peak fitting feature of the program. A 20 nm Al sample was used to calibrate the diffraction pattern by providing the camera constant. Also, the Al UED intensity decay with laser heating was used to obtain time delay zero and determine the temporal resolution of the UED setup.

3. RESULTS AND DISCUSSION

3.1. Nanoparticle Preparation. Figure 1a is a TEM of NPs fabricated by sputtering ∼20 nm In on top of ∼8 nm Al and capped with another ∼8 nm Al film resulting in the In NPs being embedded in Al. The thicknesses here are based on the deposition rate obtained from the crystal thickness monitor. We rely on the TEM images to characterize the NPs. Figure 1b is a high-resolution TEM image of an NP showing the fringe pattern from the In(101) plans of the core, while the Al shell does not show an identifiable structure. Figure 1c is a selected area electron diffraction pattern showing strong rings of tetragonal In, but without visible Al rings. The lack of observable Al diffraction rings is due to the low scattering power of Al compared to In and the structural disorder of the Al film that, from the TEM image, does not show any atomic fringes. For other samples, when we increased the total thickness of Al to larger than twice the In thickness, Al lattice fringes and diffraction rings were observed in the TEM and the electron diffraction pattern. However, for thicker Al layers, the TEM images showed that the In NPs were not fully covered by Al. Therefore, we performed the study on the samples of Al layers thinner than the In layer to assure that the In NPs were covered by Al. No In oxide was detected in the electron diffraction images from the embedded In NPs. However, when we did not cover the In NPs with the second Al layer, In oxide was present in the diffraction patterns.

Figure 1d shows the size distribution of the In NPs. Here, we measure the area of the NP and assign a diameter to it based on approximating its area as a circle. For NPs with diameters less than ∼10 nm, the TEM images do not initially show any lattice fringes. After exposure to the focused electron beam for a few minutes, the In(101) lattice fringes appear. By fitting the size distribution into a Gaussian function, we obtain that the diameter of the NPs is 29 ±14 nm with the Al shell thickness varying from ∼2.5−4.5 nm, as shown in the TEM images in Figure 1a,b. To determine the elemental composition of the NPs core and shell, point EDS analyses of the shell, as shown in Figure 1e, and of the core, as shown in Figure 1f, are obtained. After removing the Cu and C peaks that are introduced from the TEM grid, the analysis shows that the chemical composition of areas without particles is ∼99% Al and ∼1% In, while with the NPs, it is ∼90% In and ∼10% Al.

3.2. Melting and Recrystallization Under Slow Heating and Cooling. The study of melting and recrystallization under slow heating was conducted in the UED setup by operating the electron gun at a 1 kHz repetition rate while the pump beam was blocked. The samples were heated on the resistively heated sample holder. Figure 2a,b show the normalized diffraction intensity of the In(101) and In(110) diffraction orders as a function of the base temperature. The UED pattern displayed in the inset shows uniform rings due to the large number of NPs that the electron beam is diffracted from. For heating, the intensity was normalized to that at 308 K, while for cooling the intensity was normalized to that at 320 K. The heating rate was ∼1 K/min, while the cooling rate was ∼1.7 K/min from 450 to 370 K and ∼0.4 K/min from 340 to 320 K. For the In(101) order, with heating, there was a small increase in the diffraction intensity between 310 and 360 K. When a crystal was heated, the increased mean vibrational amplitude results in a decreased Bragg peak intensity due to the Debye−Waller factor. However, this is clearly not what we observe for the In(101) peak. This behavior was observed previously for In NPs and was explained by the melting of NPs with sizes smaller than 5 nm,[9] since the (101) peak overlapped with the diffraction of the most-probable nearest neighbor separation in molten In.[44] The persistence of the In(101) diffraction order for temperatures ≥450 K (T_m of In is 430 K) is consistent with this explanation.[44] Due to the In(101) peak intensity increase with heating at the lower temperature range, it is not possible to use the In(101) peak intensity in our data to obtain the Debye−Waller factor. Also, it is not accurate to use the disappearance of that peak to identify the melting point, as the In(101) diffraction ring persists as a halo at temperatures above T_m of In. We, therefore, use the inflection point of intensity drop as an indicative of the melting of most of the In NPs. This inflection point occurs at 413 K. On the other hand, for the In(110) order, the diffraction intensity decreases with temperature rise, which is consistent with the increased thermal vibrational amplitude of atoms with heating. The intensity of the In(110) peak disappears within the background at ∼411 K, a temperature very close to the inflection point observed for the In(101) peak. Therefore, we conclude that the melting point of the embedded In NPs is ∼411 K, which is ∼19 K below the bulk T_m of In.

The intensity of the Bragg diffraction peaks depends on the mean-square displacement of the atoms. Through the Debye−

https://dx.doi.org/10.1021/acs.jpcc.0c04950
J. Phys. Chem. C 2020, 124, 19340−19347

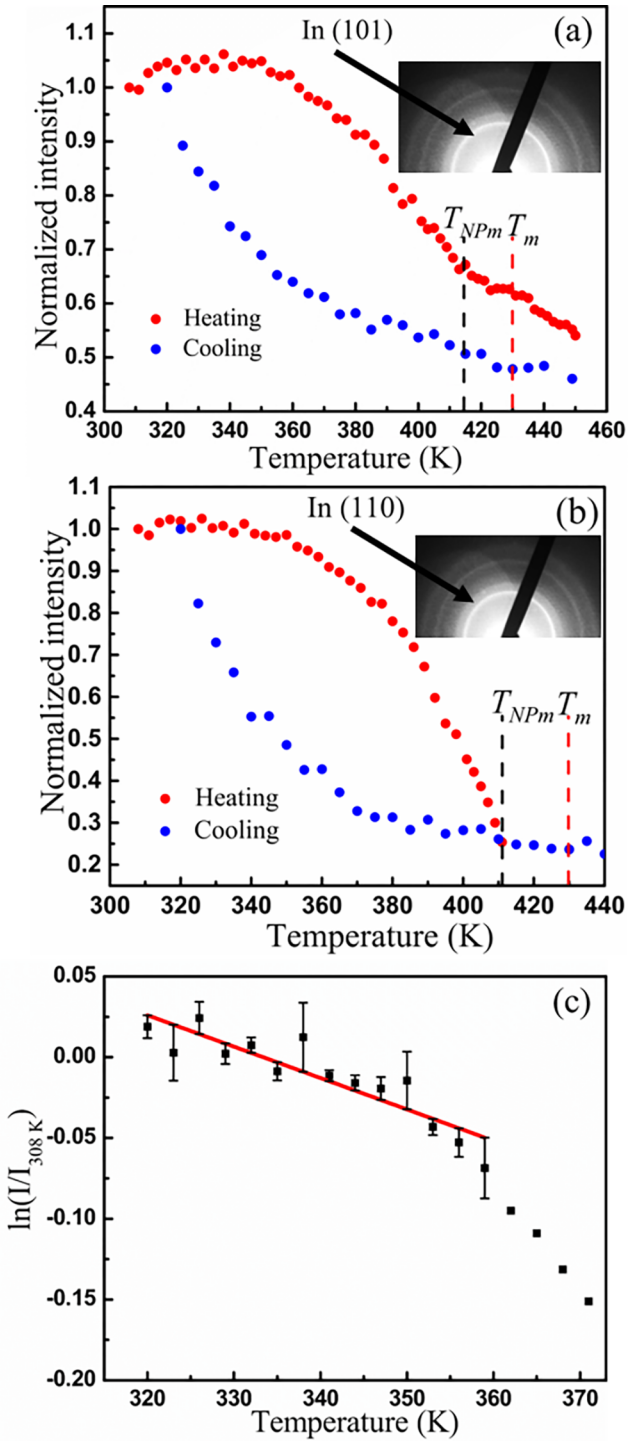

Figure 2. Diffraction intensity with temperature, (a) In(101) and (b) In(110). With heating, the intensity is normalized to that at 308 K, while with cooling the intensity is normalized to that at 320 K. The estimated melting point T_{NPm} of In(101) and (110) are 413 and 411 K, respectively, while T_m is the bulk melting point of In. (c) Natural log of In(110) intensity normalized to that at 308 K shows the deviation from the Debye–Waller exponential behavior at temperatures higher than 357 K. The solid line is a linear fit used for estimating the Debye temperature. Inset: diffraction pattern obtained at room temperature using the UED system.

Waller factor, the root-mean-square (rms) displacement of the atoms is directly related to the intensity of the Bragg peak.

$$I(G, T) = I_0(G, T) \times \exp(-2 \times M_G) \quad (1)$$

where $\mathbf{G} = \hbar(\mathbf{k}_f - \mathbf{k}_i)$ is the momentum transfer vector of the scattered electrons, and the exponential term is the Debye–Waller factor.

$$2M_G = \langle u_G^2 \rangle \times \frac{16 \times \pi^2 \times \sin^2 \theta}{\lambda^2} \quad (2)$$

where λ is the electron wavelength, θ is the scattering angle, $I_0(G,T)$ is the scattered intensity of a rigid lattice, and $\langle u_G^2 \rangle$ is the rms vibrational amplitude in the direction of the scattering vector $\mathbf{G}$. The rms vibrational amplitude can be calculated using the harmonic oscillator model in the high-temperature limit.[45]

$$\langle u_G^2 \rangle = \left(\frac{3 \times N \times \hbar^2}{M \times k_B} \right) \left[\frac{T}{\Theta_D^2} \right] \quad (3)$$

where Θ_D is the Debye temperature, M is the atomic weight of the sample, T is the base temperature, N is Avogadro's number, k_B is Boltzmann's constant, and $\hbar$ is Planck's constant divided by 2π. Therefore, we can estimate Θ_D of the embedded In NPs by applying a linear fit to the natural log of the normalized Bragg peak intensity at the lower temperature range, where the atom oscillations are harmonic. Figure 2c shows the fitting result of In(110) with the temperature up to 357 K used in the fit to calculate Θ_D, which is found to be 63 ± 9 K. The error range in Θ_D is based on the standard deviation from three separate experimental runs with three diffraction patterns obtained for each run at each temperature. This value is between 49 ± 10 K of the In(111) surface and 108 K of the bulk In.[20] The atoms in reduced dimensionality have a smaller coordination number and, consequently, have thermal vibrational amplitudes greater than that of the bulk. This results in Θ_D of surfaces and NPs to be lower than that of the bulk. However, the presence of the Al matrix in the core–shell structure could reduce the thermal vibrational amplitudes and possibly increase Θ_D from that of uncoated NPs. After NP melting, cooling the ensemble of NPs shows strong undercooling of ~80 K observable in both the In(101) and (110) diffraction orders.

The position and width of the diffraction peak are also measured with the increase of temperature. The diffraction peak's center position is related to the lattice spacing of a particular set of planes in a crystal and the peak width is, in general, related to the average size and crystallinity of the NPs. Also, inhomogeneity in the lattice spacing tends to broaden the width of the Bragg peaks. Through fitting the diffraction peaks profile by several functions, including Gaussian and Lorentzian,[40] we found that the Lorentzian function provides the best fit to our data. The center position and the FWHM of the fitted diffraction peaks are obtained by a MATLAB program and recorded at each temperature. Using Al as a calibration standard, the In peak positions can be transformed to lattice spacing d and its normalized change as a function of temperature is shown in Figure 3a. A linear lattice thermal expansion is observed for the temperature range from room temperature to 383 K for In(101) with the measured thermal expansion coefficient of $(3.22 \pm 0.17) \times 10^{-5}$ K^{-1}. For temperatures higher than 383 K, a larger thermal expansion is observed. For the In(110) planes, thermal expansion is observed up to 390 K with a linear expansion coefficient of $(6.48 \pm 0.50) \times 10^{-5}$ K^{-1}, and the lattice spacing shows little

https://dx.doi.org/10.1021/acs.jpcc.0c04950
J. Phys. Chem. C 2020, 124, 19340–19347

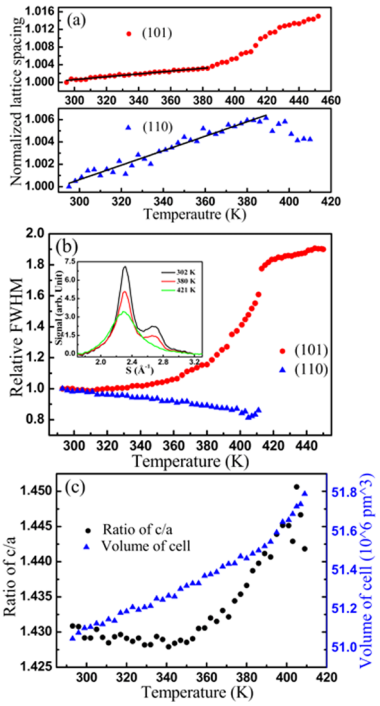

Figure 3. Analysis of diffraction peak angle and width with temperature. (a) Normalized lattice spacing. The solid lines are linear fits used to calculate the thermal expansion coefficient. (b) Relative diffraction peak width (FWHM). The inset is circularly averaged diffraction pattern showing the In(101) and In(110) peaks at different base temperatures. (c) The c/a ratio and In NP unit cell volume as a function of the base temperature.

change for temperatures higher than ∼390 K up to ∼410 K, which is the maximum temperature at which we are able to measure the lattice spacing for that peak. Anisotropy in the thermal expansion of bulk In was previously reported.[46] The result shows anisotropy in the thermal expansion of the embedded In NPs and its dependence on temperature with a smaller thermal expansion coefficient in the (101) direction up to ∼383 K. Figure 3b shows the FWHM of the diffraction peaks as a function of temperature. The FWHM of the In(101) peak has a slow increase with heating up to ∼360 K and then rapidly increases with heating over the temperature range from 360 to 420 K due to loss of long-range order. For temperatures higher than ∼411 K, the observed saturation of the In(101) peak width with temperature indicates the melting of the NPs, which is consistent with the behavior of the Bragg peak intensities shown in Figure 2. However, the change of the FWHM of the In(110) peak, where the FWHM is reduced with temperature, is unusual. This behavior could be due to the interfacial relationship of the In NPs with the Al matrix, where the Al (111) lattice spacing of 2.33 Å is almost similar to that of the In(110) of 2.30 Å. The difference in the thermal expansion coefficient of Al and In, which is also anisotropic, causes stress at the In/Al interfaces that is directional-dependent and can affect the development of melting at the interface in a manner that depends on the NP facet. For the tetragonal In unit cell with lattice parameters $a = b \neq c$, the lattice spacing of the (110) plane is only related to the lattice parameter a, while the (101) plane is determined by both a and c. Therefore, the c/a ratio and the volume of the unit cell with temperature can be calculated from the lattice spacing. Figure 3c shows the c/a ratio and the volume of the unit cell as a function of temperature. From the c/a ratio, we find that the embedded In NPs show strong anisotropic thermal expansion. A linear increase in the volume of the unit cell is observed from Figure 3c over the temperature range from 293 to ∼390 K.

3.3. Ultrafast Laser Heating and Melting. Next, we discuss the ultrafast laser heating experiments. Figure 4a shows

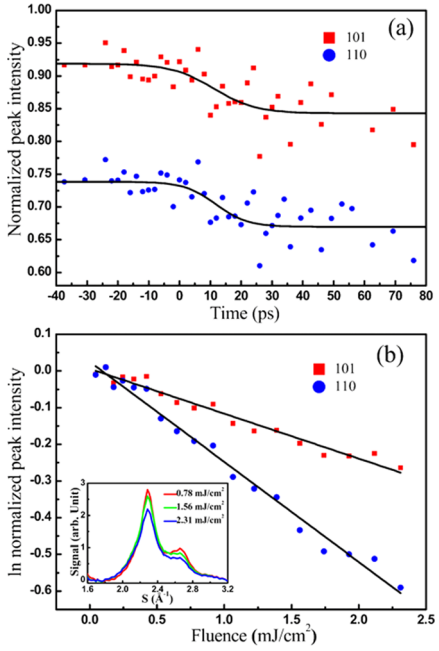

Figure 4. (a) UED scan showing the temporal change in the In(101) and In(110) peaks with laser heating starting from room temperature. (b) Natural log of the normalized peak intensity (heating laser-on/heating laser-off) as a function of laser fluence. Inset: circularly averaged diffraction pattern under different laser fluences, and the delay of the electron probe pulse from the laser heating pulse at the sample was 100 ps.

the time-resolved intensity of the In(101) and In(110) diffraction peaks when the NPs are heated with 1.6 mJ/cm^2 laser pulses starting from room temperature. By applying sigmodal fitting $= \frac{A_1 - A_2}{1 + e^{(t - t_0)/dt}} + A_2$, where I is the normalized diffraction intensity and t is the delay time, we extracted the decay time $2t_0$, which is 13.7 ± 2.0 ps for the (101) order and 10.3 ± 1.5 ps for the (110) order based on the average of three diffraction patterns. The measured different decay times of the (101) and (110) orders indicate the anisotropic electron−phonon coupling when In is excited by an ultrafast laser. This time scale represents the time of energy coupling to the phonons. For electron−phonon (e−ph) coupling, the thermalization time for many metals ranges from a few picoseconds to up to ∼10 ps when the metal is heated from room temperature.[40] This observed longer decay time is because the surrounding Al matrix is also excited by the ultrafast laser pulse and hot and thermalized electrons from Al can couple to the embedded In NPs. The absorption skin depths of Al and In at the 800 nm laser wavelength are 8 and 10 nm, respectively.[47]

The delay time between the pump laser and the probe electrons at the sample was set at 100 ps, and the diffraction patterns were obtained for different laser fluences. Figure 4b shows the natural log of the diffraction intensity, normalized to that without laser heating, as a function of laser fluence. The linear dependence of the log of the intensity ratio between

https://dx.doi.org/10.1021/acs.jpcc.0c04950
J. Phys. Chem. C 2020, 124, 19340−19347

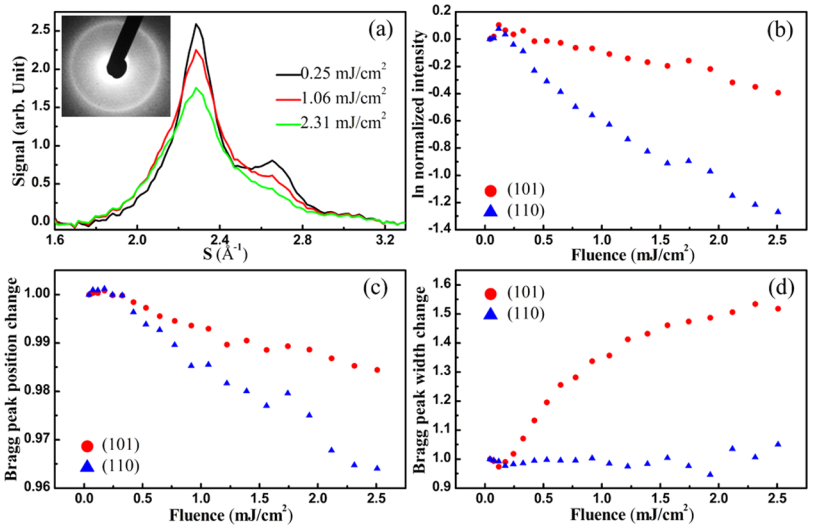

Figure 5. (a) Circularly averaged diffraction pattern of In(101) and (110) with different laser heating from a base temperature of 352 K. Inset is the diffraction pattern under 2.31 mJ/cm^2. (b) Natural log of peak intensity as a function of laser fluence. (c) Relative peak position as a function of laser fluence. (d) Relative peak width with laser fluence. The delay of the electron probe pulse from the laser heating pulse at the sample was 100 ps.

laser-on and laser-off follows what is expected from the Debye−Waller dependence with a linear increase of NP temperature with the laser fluence. Using the Debye temperature obtained from the In(110) diffraction order, obtained from Figure 2c, we can estimate the maximum lattice temperature under laser heating. Results show that the maximum In temperature increase with the fluence in Figure 3b is related to the laser fluence by 117 ± 33 K/mJ·cm^{-2}.

We then increased the base temperature to 352 K and repeated the UED study, as shown in Figure 4. At 352 K, some NPs remain in the molten state after melting by the initial laser pulse followed by cooling due to the large undercooling, as shown in Figure 2. The normalized peak intensity drop of the In(101) and In(110) peaks with temperature in Figure 5b do not show a clear deviation point from the exponential behavior based on the Debye−Waller factor. Therefore, the limits of superheating may not be directly determined by peak intensity change in this case. We look for the indications of NP melting from the change in peak position (Figure 5c) and peak width (Figure 5d). The increase in the In(101) diffraction width with the laser fluence, as shown in Figure 5d, has a sharper slope below a heating laser fluence of 1.22 mJ/cm^2 and saturates around 2.12 mJ/cm^2. This saturation can be interpreted as corresponding to the termination of the melting of the ensemble of NPs because the peak width increase is caused by the disorder of the NPs, such as the formation of a liquid shell around the NPs. Once all NPs are melted, the width reaches saturation and the diffraction pattern shows only one halo ring corresponding to the liquid state of In, which is shown as an inset in Figure 5a at a laser fluence of 2.31 mJ/cm^2. According to the relationship between the laser fluence and the lattice temperature deduced from Figure 4b and assuming uniform NP size, the maximum superheating is 170 ± 70 K, which is ∼1.40 T_m. However, the NPs have a size distribution, as shown in Figure 1d. This size distribution would cause the larger NPs (assuming spherical shape) to receive less energy per unit mass than the smaller ones and, therefore, not being heated to a temperature as high as the smaller ones. The UED experiment gives a diffraction pattern that is a superposition of diffraction from all NPs diffracting the electron beam. To account for the size distribution on the maximum observed superheating, we consider the laser fluence at the threshold where the Bragg peak width in Figure 5d deviates from a linear relation with the laser fluence. This assumption will give a lower limit on the degree of superheating. Accordingly, the initial melting fluence is 1.22 mJ/cm^2, which corresponds to the superheating of ∼65 K (1.15 T_m). This superheating range is close to that calculated by Luo et al.,[26,33] which predicted maximum superheating of bulk In under 10^{12} K/s heating rate of ∼1.3 T_m. Our results show that, for In NPs embedded in Al, a subset of the NPs is superheated by an amount in the range of 1.15−1.40 T_m when heated with the 110 fs laser pulses.

4. CONCLUSIONS

The lattice structural evolution of In NPs embedded in an Al film was studied for slow heating and ultrafast heating. The melting point of the embedded In NPs was ∼19 K lower than T_m of In under slow heating (∼1 K/min). However, for ultrafast laser heating (∼10^{15} K/s), the maximum superheating in the range of 1.15−1.40 T_m was observed for a subset of the embedded In NPs. The different melting behaviors and anisotropic thermal expansion coefficients for slow heating versus ultrafast heating were interpreted in view of the In/Al interfacial properties. The anisotropic time response of In NPs for the In(101) and (110) diffraction orders was found for NPs that are laser-heated starting from room temperature. The ultrafast laser heating of NPs embedded in a material with a higher melting point and forming a coherent interface, that is, In NPs in Al, limit surface melting. Therefore, this material structure allows the NP to achieve a high degree of superheating and can be used to test theoretical models on maximum superheating and the nature of melting at extreme heating rates.

AUTHOR INFORMATION

Corresponding Author

Hani E. Elsayed-Ali − *Applied Research Center and Department of Electrical and Computer Engineering, Old Dominion*

https://dx.doi.org/10.1021/acs.jpcc.0c04950
J. Phys. Chem. C 2020, 124, 19340−19347

University, Newport News, Virginia 23606, United States; orcid.org/0000-0002-1329-5018; Email: helsayed@odu.edu

Authors

Yueli Zhang − *Applied Research Center, Old Dominion University, Newport News, Virginia 23606, United States; School of Electronics & Information Engineering, Xi'an Jiaotong University, Xi'an 710049, China*

Hui Xiong − *Applied Research Center, Old Dominion University, Newport News, Virginia 23606, United States*

Complete contact information is available at: https://pubs.acs.org/10.1021/acs.jpcc.0c04950

Author Contributions

The manuscript was written through the contributions of all authors. All authors have given their approval to the final version of the manuscript.

Notes

The authors declare no competing financial interest.

■ ACKNOWLEDGMENTS

This study is based on research supported by the National Science Foundation under Grant No. 1708717.

■ REFERENCES

(1) Mei, Q.; Lu, K. Melting and Superheating of Crystalline Solids: From Bulk to Nanocrystals. *Prog. Mater. Sci.* **2007**, *52*, 1175−1262.
(2) Dippel, M.; Maier, A.; Gimple, V.; Wider, H.; Evenson, W.; Rasera, R.; Schatz, G. Size-Dependent Melting of Self-Assembled Indium Nanostructures. *Phys. Rev. Lett.* **2001**, *87*, No. 095505.
(3) Liu, Z.; Sui, X.; Kang, K.; Qin, S. Logarithmic Size-Dependent Melting Temperature of Nanoparticles. *J. Phys. Chem. C* **2015**, *119*, 11929−11933.
(4) Gao, F.; Gu, Z. *Melting Temperature of Metallic Nanoparticles in Handbook of Nanoparticles*; Aliofkhazraei, M., Ed.; Springer: Switzerland, 2015; pp 1−25.
(5) Li, Y.; Zang, L.; Jacobs, D. L.; Zhao, J.; Yue, X.; Wang, C. In Situ Study on Atomic Mechanism of Melting and Freezing of Single Bismuth Nanoparticles. *Nat. Commun.* **2017**, *8*, No. 14462.
(6) Buffat, P.; Borel, J. P. Size Effect on the Melting Temperature of Gold Particles. *Phys. Rev. A* **1976**, *13*, 2287−2298.
(7) Wronski, C. The Size Dependence of the Melting Point of Small Particles of Tin. *Br. J. Appl. Phys.* **1967**, *18*, 1731−1737.
(8) Coombes, C. The Melting of Small Particles of Lead and Indium. *J. Phys. F: Met. Phys.* **1972**, *2*, 441−449.
(9) Jiang, Q.; Aya, N.; Shi, F. Nanotube Size-Dependent Melting of Single Crystals in Carbon Nanotubes. *Appl. Phys. A: Mater. Sci. Process.* **1997**, *64*, 627−629.
(10) Lu, K.; Li, Y. Homogeneous Nucleation Catastrophe as a Kinetic Stability Limit for Superheated Crystal. *Phys. Rev. Lett.* **1998**, *80*, 4474−4477.
(11) Zhang, Z.; Li, J.; Jiang, Q. Modelling for Size-Dependent and Dimension-Dependent Melting of Nanocrystals. *J. Phys. D: Appl. Phys.* **2000**, *33*, 2653−2656.
(12) Frenken, J. W.; Van der Veen, J. Observation of Surface Melting. *Phys. Rev. Lett.* **1985**, *54*, 134−137.
(13) Herman, J.; Elsayed-Ali, H. Superheating of Pb (111). *Phys. Rev. Lett.* **1992**, *69*, 1228−1231.
(14) Peppiatt, S. The Melting of Small Particles. Ii. Bismuth. *Proc. R. Soc. London, Ser. A* **1975**, *345*, 401−412.
(15) Spiller, G. Time-Dependent Melting and Superheating of Lead Crystallites. *Philos. Mag. A* **1982**, *46*, 535−549.
(16) Zhang, Z.; Kulatunga, P.; Elsayed-Ali, H. Reflection High-Energy Electron-Diffraction Study of Melting and Solidification of Pb on Graphite. *Phys. Rev. B* **1997**, *56*, 4141−4148.
(17) Métois, J. J.; Heyraud, J. The Overheating of Lead Crystals. *J. Phys. France* **1989**, *50*, 3175−3179.
(18) Blackman, M.; Peppiatt, S. J.; Sambles, J. R. Superheating of Bismuth. *Nat. Phys. Sci.* **1972**, *239*, 61−62.
(19) Murphy, E.; Elsayed-Ali, H.; Herman, J. Superheating of Bi (0001). *Phys. Rev. B* **1993**, *48*, 4921−4924.
(20) Lin, B.; Elsayed-Ali, H. E. Temperature Dependent Reflection Electron Diffraction Study of in (111) and Observation of Laser-Induced Transient Surface Superheating. *Surf. Sci.* **2002**, *498*, 275−284.
(21) Zhang, D.; Cantor, B. Melting Behaviour of in and Pb Particles Embedded in an Al Matrix. *Acta Metall. Mater.* **1991**, *39*, 1595−1602.
(22) Zhong, J.; Zhang, L.; Jin, Z.; Sui, M.; Lu, K. Superheating of Ag Nanoparticles Embedded in Ni Matrix. *Acta Mater.* **2001**, *49*, 2897−2904.
(23) Lu, K.; Jin, Z. Melting and Superheating of Low-Dimensional Materials. *Curr. Opin. Solid State Mater. Sci.* **2001**, *5*, 39−44.
(24) Goswami, R.; Chattopadhyay, K. Melting of Bi Nanoparticles Embedded in a Zn Matrix. *Acta Mater.* **2004**, *52*, 5503−5510.
(25) Lopeandía, A. F.; Rodriguez-Viejo, J. Size-Dependent Melting and Supercooling of Ge Nanoparticles Embedded in a Sio2 Thin Film. *Thermochim. Acta* **2007**, *461*, 82−87.
(26) Luo, S.-N.; Ahrens, T. J. Shock-Induced Superheating and Melting Curves of Geophysically Important Minerals. *Phys. Earth Planet. Inter.* **2004**, *143*−*144*, 369−386.
(27) Stringe, M.; Rösner, H.; Wilde, G. Effect of High Heating Rates on the Melting Behavior of Embedded in Nanoparticles. *Thermochim. Acta* **2019**, *677*, 206−210.
(28) Geiger, F.; Busse, C.; Loehrke, R. The Vapor Pressure of Indium, Silver, Gallium, Copper, Tin, and Gold between 0.1 and 3.0 Bar. *Int. J. Thermophys.* **1987**, *8*, 425−436.
(29) Giessen, B. C.; Morris, M.; Grant, N. J. Metastable Indium-Bismuth Phases Produced By Rapid Quenching. *AIME Met. Soc. Trans.* **1967**, *239*, 883−889. ICDD PDF Card No.: 03-065-7421.
(30) Van der Veen, J. F.; Pluis, B.; Denier van der Gon, A. W. *Surface Melting in Chemistry and Physics of Solid Surfaces Vii*; Van Hove, M.; Howe, R.; Vanselow, R., Eds.; Springer-Verlag: Berlin, 1988; pp 455−490.
(31) Zhang, M.; Efremov, M. Y.; Schiettekatte, F.; Olson, E.; Kwan, A.; Lai, S.; Wisleder, T.; Greene, J.; Allen, L. Size-Dependent Melting Point Depression of Nanostructures: Nanocalorimetric Measurements. *Phys. Rev. B* **2000**, *62*, 10548−10557.
(32) Sheng, H.; Ren, G.; Peng, L.; Hu, Z.; Lu, K. Epitaxial Dependence of the Melting Behavior of in Nanoparticles Embedded in Al Matrices. *J. Mater. Res.* **1997**, *12*, 119−123.
(33) Luo, S.-N.; Ahrens, T. J.; Çağın, T.; Strachan, A.; Goddard, W. A., III; Swift, D. C. Maximum Superheating and Undercooling: Systematics, Molecular Dynamics Simulations, and Dynamic Experiments. *Phys. Rev. B* **2003**, *68*, No. 134206.
(34) Herman, J. W.; Elsayed-Ali, H. Time-Resolved Structural Studies of the Low-Index Faces of Lead. *Phys. Rev. B* **1994**, *49*, 4886−4897.
(35) Zhang, D.; Cantor, B. Heterogeneous Nucleation of in Particles Embedded in an Ai Matrix. *Philos. Mag. A* **1990**, *62*, 557−572.
(36) Zhang, L.; Jin, Z.; Zhang, L.; Sui, M.; Lu, K. Superheating of Confined Pb Thin Films. *Phys. Rev. Lett.* **2000**, *85*, 1484−1487.
(37) Olson, E.; Efremov, M. Y.; Zhang, M.; Zhang, Z.; Allen, L. Size-Dependent Melting of Bi Nanoparticles. *J. Appl. Phys.* **2005**, *97*, No. 034304.
(38) Wang, F.; Wang, Z.; Peng, Y.; Zheng, Z.; Han, Y. Homogeneous Melting near the Superheat Limit of Hard-Sphere Crystals. *Soft Matter* **2018**, *14*, 2447−2453.
(39) Ruan, C.-Y.; Murooka, Y.; Raman, R. K.; Murdick, R. A. Dynamics of Size-Selected Gold Nanoparticles Studied by Ultrafast Electron Nanocrystallography. *Nano Lett.* **2007**, *7*, 1290−1296.
(40) Nie, S.; Wang, X.; Li, J.; Clinite, R.; Cao, J. Femtosecond Electron Diffraction: Direct Probe of Ultrafast Structural Dynamics in Metal Films. *Microsc. Res. Tech.* **2009**, *72*, 131−143.

(41) Qian, B. L.; Elsayed-Ali, H. E. Electron Pulse Broadening Due to Space Charge Effects in a Photoelectron Gun For Electron Diffraction and Streak Camera Systems. *J. Appl. Phys.* **2002**, *91*, 462−468.
(42) Esmail, A. R.; Bugayev, A.; Elsayed-Ali, H. E. Electron Diffraction Studies of Structural Dynamics of Bismuth Nanoparticles. *J. Phys. Chem. C* **2013**, *117*, 9035−9041.
(43) Ramos, P. M.; Ruisánchez, I. Noise and Background Removal in Raman Spectra of Ancient Pigments Using Wavelet Transform. *J. Raman Spectrosc.* **2005**, *36*, 848−856.
(44) Orton, B.; Smith, S. P. An X-Ray Diffraction Investigation of Liquid Indium. *Philos. Mag.* **1966**, *14*, 873−877.
(45) Goodman, R.; Farrell, H.; Somorjai, G. Mean Displacement of Surface Atoms in Palladium and Lead Single Crystals. *J. Chem. Phys.* **1968**, *48*, 1046−1051.
(46) Smith, J.; Schneider, V. Anisotropic Thermal Expansion of Indium. *J. Less-Common Met.* **1964**, *7*, 17−22.
(47) Mathewson, A.; Myers, H. Absolute Values of the Optical Constants of Some Pure Metals. *Phys. Scr.* **1971**, *4*, 291−292.

https://dx.doi.org/10.1021/acs.jpcc.0c04950
J. Phys. Chem. C 2020, 124, 19340−19347